# Supporting Information for Machine learning based prediction of channelisation during dissolution of carbonate rocks

F, Brondolo[1,2,3], P. A. Cilli[1,2,4], I. B. Butler[1,2], A. Fraser-Harris[1,2],K. Edlmann[1,2]and C. McDermott[1,2]

[1]School of Geosciences, University of Edinburgh, Edinburgh, UK

[2]International Centre for Carbonate Reservoirs, Edinburgh, UK

[3]Now at Stanford University - SLAC, Menlo Park, USA

[4]Now at Department of Earth Sciences, University of Oxford, Oxford, UK

## Contents of this file

1. Text

2. Figures S1 to S9

3. Tables S1 to S2

## Introduction

The text provides additional details on the preparation process for the rock samples, the µCT data and their processing, the software used to process the µCT data. Additional information are given regarding the variables processed by the artificial neural network solution, and their computation by our bespoke software.

**Sample Characteristics**

We used travertine rocks, whose formation and morphology were first introduced in the 1960' (Kitano, 1963), and further studied by various authors (Marques Erthal, 2018; Chafetz & Folk, 1984; Pentecost, 1990; Guo & Riding, 1992, 1994, 1998; Chafetz & Guidry, 1999; Kele et al., 2008; Jones & Renaut, 2010; Wright, 2012; Chafetz, 2013; Chitale et al., 2015; Wright & Barnett, 2015; Claes et al., 2017; Erthal et al., 2017; Fouke et al., 2000; Soete et al., 2015; Yagiz, 2009). Travertine rocks are considered good proxies for the upper Pre-salt reservoir rock (shrub framestone) due to petromorphological resemblance between both formations (Marques Erthal, 2018; Claes et al., 2017; Virgone et al., 2013; Borghi et al., 2013; Schröder et al., 2016; Rezende & Pope, 2015; Soete et al., 2015; Chitale et al., 2015; Boyd et al., 2015). Travertines are carbonate formations deposited in lacustrine environments. They are structured in millimetres to centimetres layers of $CaCO_3$ expending upwards. They are highly heterogeneous and can be brittle depending on the burial history of each sample. All four samples' geometrical and physical properties are presented in Table S1. For this study, the core samples have been sourced from large blocs of travertines (shrub layer, sampled from Saturnia Italy).

Travertines are mainly made of calcium; usually $> 90\%CaCO_3$ (Pentecost, 2005). The secondary principal element is magnesium which substitutes Ca and can be found under the form of calcite magnesian, dolomite, or montmorillonite ($(Ca,Mg)CO_3$) in low quantities (Chafetz & Folk, 1984; Pentecost, 2005; Kele et al., 2008; Erthal et al., 2017). The results of an XRD analysis ran on our block of travertines are shown in Table S2.

Figure S1 shows µCT slices taken from each core sample used in this work. The porous media is composed of heterogeneously distributed pores, whose size and shape appeared

to widely vary throughout a slice. A ($LFRLES$ sample) and B ($MFRHES$ sample) displayed a mixture of shrubby porosity coupled with coated bubbles which have been formed due to degassing during the precipitation of the calcite. Both samples evolved towards the shrubby structures seen in C ($HFRHES$ sample) and D ($HFRLES$ sample), which displayed elongated pores and dendritic calcite crystals (not seen under µCT imaging) (Ronchi & Cruciani, 2015).

**µCT Imaging Acquisition**

Fluids injected through carbonate rocks generate dissolution that physically relates to the formation of wormholes. They are preferential flow-paths that increase fluid conductivity and allow the injection fluid to flow more easily from one end of the sample to another (Hoefner & Fogler, 1988; Fredd & Fogler, 1998; Golfier et al., 2002). These changes in the rock matrix can be detected using µCT scanning acquisition and post-processing of the images, by arithmetically comparing the pre- and post-experimental datasets. The µCT facility of the University of Edinburgh has been used for qualitative and quantitative analyses of these post-flooding damages. A reconstructed volume provides us with a 3D map of absorbed light due to the difference in density of the matrix of a rock (Landis & Keane, 2010). For each core, pre- and post-experimental flooding tomographic data were acquired at ∼130 kV, and ∼25 W target power loading, with a copper energy filter. A rotary stage is placed on top of an adjustable screw, which allowed the scans of different parts of a sample by adjusting its elevation. The instrument had a conventional cone-beam configuration with a Feinfocus 10-160 kV dual transmission/reflection source, a MICOS UPR-160 air

bearing rotary stage and a Perkin Elmer XRD 0822 amorphous silicon 1 MP flat-panel camera with a terbium-doped gadolinium oxysulfide scintillator. The geometry of the cone-beam window was approximately 3 cm wide, which can be less than the length of the cores, therefore each scan of a whole sample was split into two to three sections. Scans consisted of 2,000 projections; each of 2 s duration, during a 360° revolution. They were first recorded as 2D TIFF of projected images, followed by tomographic reconstructions into 3D stacks. Further details about acquisition and reconstruction processes along with the underlying physics of µCT scanning can be found in various studies (Landis & Keane, 2010; Salvo et al., 2010). For each section, reconstruction by filtered back-projection was done by using Octopus v8.7 software (Dierick et al., 2004), while post-processing data analysis was done through Fiji (Schindelin et al., 2012) and Avizo® 9 functions (`https://www.thermofisher.com/uk/en/home/industrial/electron-microscopy/electron-microscopy-instruments-workflow-solutions/3d-visualization-analysis-software.html`).

## Additional Information on µCT Imaging Processing

The reconstruction stage of the projected images was done using Octopus v8.7 (`https://octopusimaging.eu/`). Back processing, registration, and analysis were done via Avizo® 9, using the Image Registration Wizard and the Merge tool. Image Registration Wizard assists the user into registering several 3D volumes by mathematically enclosing the overlap between them while the Merge function combines the stacks into one set of data. Our methodology involved the registration of both unaltered (pre-experimental) and altered (post-experimental) datasets into the same 3D space,

allowing us to further subtract both stacks to account for potential differences. As such, we used several tools in Avizo® 9: the Arithmetic operator, Interactive Thresholding, Label Analysis, and the Analysis Filter function. The Arithmetic operator applies a mathematical condition on the input 16-bit datasets; here we wanted to have the absolute difference between the pre- and post-experimental dataset. The Interactive Thresholding module differentiates the volumes based on the intensity values of the raw images. Thresholding was applied over the entire volume, and a voxel was set to black if its intensity $I_{ij}$ is less than a fixed value $T$ set by the user, so that $I_{ij} > T = 1$ and $I_{ij} < T = 0$. The Label Analysis function creates a connected network of voxels depending on their 3D arrangement, i.e. whether they are connected by their sides, corners, or faces. Finally, we used the Analysis Filter which applies a user-defined filter over any geometrical parameter of the 3D volume. We filtered our dataset to isolate the main parts of the channels by removing 3D volumes smaller than a certain amount of voxels. The drawback of imaging 38 mm diameter large samples relies on acquiring the images at a lower resolution, against the high energy needed to scan through the entire sample. As a result, our volumes displayed a voxel side length of 40 µm, which was enough to resolve most of the features that could be expected in these kinds of studies, but too large to obtain a detailed picture of the microporosity.

**µCT Imaging Output Data**

µCT images have been obtained on dry samples, before and after each experimental flooding. The core samples have been cleaned for ∼15 min in a sonic bath, after the coring/cutting phases and after the flooding stage, to drive the remaining seawater out

the sample. These extra steps have allowed us to obtain clearer outputs from the µCT scanning. The reconstruction process produced ∼2.5 GB 16-bit greyscale images.

The shape and spread of a wormhole have been calculated by evaluating the density of nodes per region of ∼0.01 $cm^2$. A wormhole formation expands and branches as the injection rate is increased (Siddiqui et al., 2006) implying that the thickness of a wormhole should then be primarily linked to the forcing of the fluid. In this work, we have isolated the main wormholes and branches.

**µCT Images: Pre-processing**

The pre-processor used in this work is an evolving solution developed over the entire course of this study and is usually referred to as the "ICCR-Macropore". It has been used in two ways:

- As a processor of macro structures of 2D slices. It performed geometrical calculations based on the images and generated spreadsheets which were used for further analysis.
- As a data pre-processor of the OGS software (Kolditz et al., 2012). It generated 2D mesh files of the slices for further HMC modelling. Figure S4 shows an example of input file for OGS used.

The solution uses 2D slices taken from 3D volumes of the image stacks. The volumes were rendered by the µCT scan of a rock sample while the reconstruction process of the 3D rendering was done under Fiji (Schindelin et al., 2012) and Avizo® 9.

**Pre-processor Software: Numerical Structure of a Pore**

The interpretation of an SVG file (converted TIFF files) by the ICCR-Macropore creates instances or objects. Figure S2 is a simplified Unified Modelling Language (UML) diagram displaying the relationship between the different classes. At this stage, a pore is interpreted as a polygon; a polygon is comprised of nodes, referred to as points; each pair of point forms a line. These classes belong to a single project. The relationship between classes can be summarized as follows:

- A project contains 1 to $n$ Polygon(s).
- A polygon belongs to 1 Project only and is made of $n$ Point(s).
- A point belongs to 1 Polygon only.
- A line is made of 2 Points, and can only belong to 1 Polygon.

**Pre-processor Software: Numerical Analysis Workflow**

Figure S3 presents the general workflow for using the tool. Four types of input file are necessary (further developed in Section "Pre-processor software: Input files"). The tool offers three options: option 1) and 2) process one or more orthogonal slices, while option 3) observes the evolution of porosity and area of the pores of a 2D image stack in the axial direction. Along with the above-mentioned geometrical analysis, the ICCR-Macropore also creates .GEO and .GLI files of the scanned slices, which are inputs for OGS.

**Pre-processor Software: Input Files**

The input files are described as follows:

- CNT file: this file is the control file. It contains interpretive and boundary variables. This user-defined file is read by the executable before analysing each image and defines how finely the images should be interpreted.

• SVG file(s): an SVG file is an XML-based vectorized image. The well-documented encoding system allowed us to create reading functions capable of extracting the geometrical data of a 2D slice such as the contour of the pores, their positions, the size of the picture, and the differentiation between pores and background rock matrix. The input picture could take the form of a picture of a clean-cut of a rock or a slice of a 3D volume of a core sample. Each picture was further binarized and converted into an SVG file.

• Comm file: the comm file is a communication file used by the Slice Picker (further described in Section "Slice Picker Software").

• Slice text files: they contain the names of the SVG files that should be processed by the ICCR-Macropore, and take the form of two text files for the two sampled orthogonal direction (X_input.txt and Y_input.text).

**Pre-processor Software: Output Files**

The tool can extract data from an SVG file format according to the user-defined settings. It produces the following files:

• data.geo is used for meshing a slice (Figure S4). A GEO file can be further edited using Gmesh (Geuzaine & Remacle, 2009), before producing the mesh for modelling purposes. The data.geo file is further used as a mechanical mesh (eg. in Section "Example of 2D analysis of fluid flow").

• data1D2D.geo is used for meshing the links between pores (Figure S7). Similar to the "data.geo" file, the links between pores can be edited and adjusted under Gmesh (Geuzaine & Remacle, 2009) before being meshed. The theory behind link generation is described in Section "Pre-processor software: Ellipse simplification".

• svg.gli is used in OGS (Kolditz et al., 2012) to connect the meshes with the desired system of equations that calculates a solution. The .gli file represents the geometry of the mesh (under the form of points and polylines). These geometric objects connect the mesh to the rest of the OGS code, calculating the solution. An example of such work is given in Section "Example of 2D analysis of fluid flow"

• Geometrical attributes: they are the results of mathematical interpretation of the polygons analysed by the ICCR-Macropore functions. Each of the attributes of interest is described in Section "Pre-processor software: Geometrical attributes".

**Pre-processor Software: Geometrical Attributes**

**Area of each pore:** The area of each pore is calculated from any irregularly shaped polygon. Each polygon's perimeter being formed by points of known coordinates $(x, y)$, we use the following formula for Area calculation:

$$a = \left| \frac{(x_1 y_2 - y_1 x_2) + (x_2 y_3 - y_2 x_3) ... + (x_n y_1 - y_n x_1)}{2} \right| \tag{1}$$

**Pore perimeter:** The perimeter of irregularly shaped pores is calculated using the distances between each pair of point $(x_1, y_1)$ and $(x_2, y_2)$, so that:

$$d = \sqrt{(x_1 - x_2)^2 + (y_1 - y_2)^2} \tag{2}$$

**Coefficient A (major axis):** The coefficient A represents the largest axis of an ellipse shape of a pore (Figure S5).

**Coefficient B (minor axis):** The coefficient B represents the smallest axis of the ellipse shape of a pore and is perpendicular to the major axis (Figure S5).

**D and l:** D and l parameters are the average width and height of each pore, plus the average width and height of the entire porosity of slice.

**Distances:** This file contains a summary of the distance between each pore. Each pore is defined by a centre point of coordinate $(x, y)$, while the distance between two pores is computed using the same function as for the pore perimeter.

**Ellipse perimeter:** The perimeter of an ellipse is calculated using Ramanujan's approximation (Ramanujan, 1914), and is expressed as follows:

$$\begin{aligned} h &= \frac{(a-b)^2}{(a+b)^2} \\ p &\approx \pi(a+b)\left(1+\frac{3h}{10+\sqrt{4-3h}}\right) \end{aligned} \tag{3}$$

with $a$ and $b$ being the major and minor axis of the ellipse. This formula has been chosen due to its very good approximation of near-circular ellipses while being very simple to implement.

**Ratio:** Per 2D slice scanned, the ICCR-Macropore generates an excel file which contains all aspect ratios $(a/b)$ of all ellipses (pores) present on that slice.

**Pre-processor Software: Ellipse Simplification**

The ICCR-Macropore has been developed as a 2D interpreter of pore network. This network, generated for each scanned slice and saved under the "data1D2D.geo" file, relies on the arrangement and overlap state of the 2D porosity: each pore of a 2D slice is virtually replaced by an ellipse of equivalent area, shape, and orientation. Studies have simplified the complex structure of the pores by the ellipse equivalent shape of a pore (Fournier et al., 2011), while (Tsukrov & Kachanov, 1993) demonstrated that elongated pores could be replaced by their ellipse-equivalent shape for DEM modelling. Although we have not done any DEM modelling, we assume that the ellipse shape has a similar impact on the surrounding pores. The ellipses generated by the ICCR-Macropore are

enlarged by a factor controlled by the user and defined as the *area of influence* and set constant for the entire sample analysis. This factor is a 2D computational way of representing the 3D hydro-geological influence of a pore over its surrounding area. Figure S5 presents a simplified workflow for pore connection detection. The overlap-detection function of ICCR-Macropore uses the geometrical attributes of an ellipse: knowing that the sum of the distances between the foci $F_{1,2}$ and any point of the ellipse $E_1$ is a constant $C_1$, we assume that if the distance between foci of $E_1$ and any point of a second ellipse $E_2$ is less than $C_1$, then $E_2$ overlaps $E_1$, leading to the creation of a link, referred to as "Line" in Figure S2, between those two pores. A link is a 2D representation of a potential connection in 3D, while the 2D arrangement of a set of links symbolizes the pore network of a 2D slice (Figure S7). The ellipse simplification has the advantage of avoiding corner effects that can be encountered by a rectangular simplification against more resource-consuming processing. Figure S6 shows an example of artefact produced during link detection between two pores: we observe that replacing the pores by rectangular shapes (case A) would have developed a connection (represented by a blue area) where case B does not detect any.

The materialized links are displayed in Figure S7. For this example, a slice has been analysed three times, using three different *area of influence*. As observed in Figure S7-Left, a small factor of 5 only connected the larger pores, which had a large influence on their nearest neighbours. In Figure S7-Middle, a factor of 10 was applied on the same slice. In this case, most of the larger vugs were connected, while the microporosity began to be part of the global hydraulic network. No connection between the top and bottom of the slice is detected yet. With Figure S7-Right, we saw that almost all pores were part

of a network. Only the ones sitting where the rock matrix is most present are avoided, highlighting the poor influence of rock matrix and microporosity during water flooding. The larger vugs have created a bottom-to-top connection.

**Slice Picker Software**

The Slice Picker is a software written in C++ and specifically developed as a pre-processor for the Artificial Neural Network study, by generating a pre-formatted dataset of variables. The software is based on the ICCR-Macropore main functions.

The following files are needed to run the Slice Picker (Figure S8):

- The executable of the ICCR-Macropore, along with the input files needed for a correct use of the software.
- The Comm file. The "Status" variable should be set to 0 before running the Slice Picker.
- The "Slices" text file, which should contain the names of the files to be analysed.

The Slice Picker generates a formatted excel spreadsheet containing 18 variables, further used by the neural network solution, plus 1 variable (In/Out connection). The In/Out connection is a Boolean offering a rapid and alternative way to control whether a breakthrough might occur on a 2D slice of a pre-experimental scan of a rock. The function, compiled within the executable of the ICCR-Macropore, can only be triggered through the use of the Slice Picker and is based on the recursive analysis of the connected network of pores, based on the *area of influence*. The variable is set to 1 if at least one route connects the bottom of the slice to the top, and 0 otherwise.

**Slice Picker & ICCR-Macropore Interactions**

The "Status" variable of the Comm file guides both software into splitting tasks (Figure S9). A Comm status of 0 indicates a running Slice Picker, while a Comm status of 1 puts the Slice Picker in a stand-by mode during which the ICCR-Macropore processes the current 2D slice through a set of available and hidden functions only triggered through the use of the Slice Picker. Once done with the slice processing, the ICCR-Macropore updates the Comm file accordingly and closes itself, while the Slice Picker saves the set of 18 + 1 variables in a vector. The process continues until each slice has been analysed, after which an excel spreadsheet containing all the data gathered by the coupled solution is generated.

**Acknowledgments.** The authors would like to thank Petrobras and Shell for their sponsorship of the International Centre for Carbonate Reservoirs (ICCR), and for permission to publish this work from the GeoMeChem project.

The data used in this work are available at the following address: `https://doi.org/10.6084/m9.figshare.c.5335454` (Brondolo et al., 2021).

**References**

Borghi, L., Corbett, P. W., et al. (2013). Lacustrine carbonates-for the purpose of reservoir characterization are they different? In *Otc brasil.*

Boyd, A., Souza, A., Carneiro, G., Machado, V., Trevizan, W., Santos, B., ... others (2015). Presalt carbonate evaluation for santos basin, offshore brazil. *Petrophysics*, *56*(06), 577–591.

Brondolo, F., Cilli, P., Fraser-Harris, A., Butler, I., Edlmann, K., & Mc-

Dermott, C. (2021, Mar). *Machine learning based prediction of channelisation during dissolution of carbonate rocks.* figshare. Retrieved from https://figshare.com/collections/Machine_learning_based_prediction_of_channelisation_during_dissolution_of_carbonate_rocks/5335454/1 doi: 10.6084/m9.figshare.c.5335454

Chafetz, H. S. (2013). Porosity in bacterially induced carbonates: Focus on microporesmicroporosity after bacterial decay. *AAPG bulletin*, *97*(11), 2103–2111.

Chafetz, H. S., & Folk, R. L. (1984). Travertines; depositional morphology and the bacterially constructed constituents. *Journal of Sedimentary Research*, *54*(1), 289–316.

Chafetz, H. S., & Guidry, S. A. (1999). Bacterial shrubs, crystal shrubs, and ray-crystal shrubs: bacterial vs. abiotic precipitation. *Sedimentary Geology*, *126*(1-4), 57–74.

Chitale, V. D., Alabi, G., Gramin, P., Lepley, S., Piccoli, L., et al. (2015). Reservoir characterization challenges due to the multiscale spatial heterogeneity in the presalt carbonate sag formation, north campos basin, brazil. *Petrophysics*, *56*(06), 552–576.

Claes, H., Erthal, M. M., Soete, J., Özkul, M., & Swennen, R. (2017). Shrub and pore type classification: Petrography of travertine shrubs from the ballık-belevi area (denizli, sw turkey). *Quaternary International*, *437*, 147–163.

Dierick, M., Masschaele, B., & Van Hoorebeke, L. (2004). Octopus, a fast and user-friendly tomographic reconstruction package developed in labview®. *Measurement Science and Technology*, *15*(7), 1366.

Erthal, M. M., Capezzuoli, E., Mancini, A., Claes, H., Soete, J., & Swennen, R. (2017). Shrub morpho-types as indicator for the water flow energy-tivoli travertine case (cen-

tral italy). *Sedimentary geology*, *347*, 79–99.

Fouke, B. W., Farmer, J. D., Des Marais, D. J., Pratt, L., Sturchio, N. C., Burns, P. C., & Discipulo, M. K. (2000). Depositional facies and aqueous-solid geochemistry of travertine-depositing hot springs (angel terrace, mammoth hot springs, yellowstone national park, usa). *Journal of Sedimentary Research*, *70*(3), 565–585.

Fournier, F., Leonide, P., Biscarrat, K., Gallois, A., Borgomano, J., & Foubert, A. (2011). Elastic properties of microporous cemented grainstones. *Geophysics*, *76*(6), E211–E226.

Fredd, C. N., & Fogler, H. S. (1998). Influence of transport and reaction on wormhole formation in porous media. *AIChE journal*, *44*(9), 1933–1949.

Geuzaine, C., & Remacle, J.-F. (2009). Gmsh: A 3-d finite element mesh generator with built-in pre-and post-processing facilities. *International journal for numerical methods in engineering*, *79*(11), 1309–1331.

Golfier, F., Zarconne, C., Bazin, B., Lenormand, R., Lasseux, D., & QUINTARD, M. (2002). On the ability of a darcy-scale model to capture wormhole formation during the dissolution of a porous medium. *Journal of fluid Mechanics*, *457*, 213–254.

Guo, L., & Riding, R. (1992). Aragonite laminae in hot water travertine crusts, rapolano terme, italy. *Sedimentology*, *39*(6), 1067-1079.

Guo, L., & Riding, R. (1994). Origin and diagenesis of quaternary travertine shrub fabrics, rapolano terme, central italy. *Sedimentology*, *41*(3), 499–520.

Guo, L., & Riding, R. (1998). Hot-spring travertine facies and sequences, late pleistocene, rapolano terme, italy. *Sedimentology*, *45*(1), 163–180.

Hoefner, M., & Fogler, H. S. (1988). Pore evolution and channel formation during flow

and reaction in porous media. *AIChE Journal*, *34*(1), 45–54.

Jones, B., & Renaut, R. W. (2010). Calcareous spring deposits in continental settings. *Developments in Sedimentology*, *61*, 177–224.

Kele, S., Demény, A., Siklósy, Z., Németh, T., Tóth, M., & Kovács, M. B. (2008). Chemical and stable isotope composition of recent hot-water travertines and associated thermal waters, from egerszalók, hungary: Depositional facies and non-equilibrium fractionation. *Sedimentary Geology*, *211*(3-4), 53–72.

Kitano, Y. (1963). Geochemistry of calcareous deposits found in hot springs. *The Journal of earth sciences, Nagoya University*, *11*(1), 68–100.

Kolditz, O., Bauer, S., Bilke, L., Bottcher, N., Delfs, J., Fischer, T., ... Zehner, B. (2012, 9 1). Opengeosys: an open-source initiative for numerical simulation of thermo-hydro-mechanical/chemical (thm/c) processes in porous media. *Environmental Earth Sciences*, *67*(2), 589–599. doi: 10.1007/s12665-012-1546-x

Landis, E. N., & Keane, D. T. (2010). X-ray microtomography. *Materials characterization*, *61*(12), 1305–1316.

Marques Erthal, M. (2018). *Travertine shrub structures: origin, diagenetic modifications and petrophysical characteristics - tivoli case (central italy).* Retrieved from `https://lirias.kuleuven.be/retrieve/487062$$DMarcelleMarques_Thesis.pdf`

Pentecost, A. (1990). The formation of travertine shrubs: mammoth hot springs, wyoming. *Geological Magazine*, *127*(2), 159–168.

Pentecost, A. (2005). *Travertine*. Springer Science & Business Media.

Ramanujan, S. (1914). Modular equations and approximations to $\pi$. *Quart. J. Math*, *45*, 350–372.

Rezende, M., & Pope, M. (2015). Importance of depositional texture in pore characterization of subsalt microbialite carbonates, offshore brazil. *Geological Society, London, Special Publications*, *418*, SP418–2.

Ronchi, P., & Cruciani, F. (2015). Continental carbonates as a hydrocarbon reservoir, an analog case study from the travertine of saturnia, italy. *AAPG Bulletin*, *99*(4), 711–734.

Salvo, L., Suéry, M., Marmottant, A., Limodin, N., & Bernard, D. (2010). 3d imaging in material science: Application of x-ray tomography. *Comptes Rendus Physique*, *11*(9-10), 641–649.

Schindelin, J., Arganda-Carreras, I., Frise, E., Kaynig, V., Longair, M., Pietzsch, T., ... others (2012). Fiji: an open-source platform for biological-image analysis. *Nature methods*, *9*(7), 676.

Schröder, S., Ibekwe, A., Saunders, M., Dixon, R., & Fisher, A. (2016). Algal–microbial carbonates of the namibe basin (albian, angola): implications for microbial carbonate mound development in the south atlantic. *Petroleum Geoscience*, *22*(1), 71–90.

Siddiqui, S., Nasr-El-Din, H. A., & Khamees, A. A. (2006). Wormhole initiation and propagation of emulsified acid in carbonate cores using computerized tomography. *Journal of Petroleum Science and Engineering*, *54*(3-4), 93–111.

Soete, J., Kleipool, L. M., Claes, H., Claes, S., Hamaekers, H., Kele, S., ... Swennen, R. (2015). Acoustic properties in travertines and their relation to porosity and pore types. *Marine and Petroleum Geology*, *59*, 320–335.

Tsukrov, I., & Kachanov, M. (1993). Solids with holes of irregular shapes: effective moduli and anisotropy. *International Journal of Fracture*, *64*(1), R9–R12.

Virgone, A., Broucke, O., Held, A.-E., Lopez, B., Seard, C., Camoin, G., ... others (2013). Continental carbonates reservoirs: the importance of analogues to understand presalt discoveries. In *Iptc 2013: International petroleum technology conference.*

Wright, V. P. (2012). Lacustrine carbonates in rift settings: the interaction of volcanic and microbial processes on carbonate deposition. *Geological Society, London, Special Publications*, *370*, SP370–2.

Wright, V. P., & Barnett, A. J. (2015). An abiotic model for the development of textures in some south atlantic early cretaceous lacustrine carbonates. *Geological Society, London, Special Publications*, *418*, SP418–3.

Yagiz, S. (2009). Predicting uniaxial compressive strength, modulus of elasticity and index properties of rocks using the schmidt hammer. *Bulletin of Engineering Geology and the Environment*, *68*(1), 55–63.

| Sample | Length (mm) | Diam. (mm) | $\phi$ (%) | $V_p$ (cm$^3$) | $V_s$ (cm$^3$) |
|---|---|---|---|---|---|
| $HFRHES$ | 71.58 | 38 | 7.57 | 6.20 | 75.71 |
| $HFRLES$ | 68.68 | 38 | 7.65 | 5.96 | 72.01 |
| $MFRHES$ | 73.39 | 38 | 7.11 | 5.89 | 76.94 |
| $LFRLES$ | 81.2 | 38 | 5.64 | 5.2 | 86.99 |

**Table S1.** Petrological characteristics of the samples. The volume of solid was calculated from the difference between the volume of the cylindrical core and the volume of pore: $V$ - $V_p$.

| Compound | Sample 1 (%) | Sample 2 (%) |
|---|---|---|
| Calcite | 95.15 | 95.02 |
| Calcite magnesian | 4.41 | 4.02 |
| Dolomite | 0.24 | 0.47 |
| Quartz | 0.1 | 0.1 |
| Montmorillonite | 0.1 | 0.4 |

**Table S2.** Chemical composition of a block of travertine (Saturnia Italy). Data from a in-house XRD analysis.

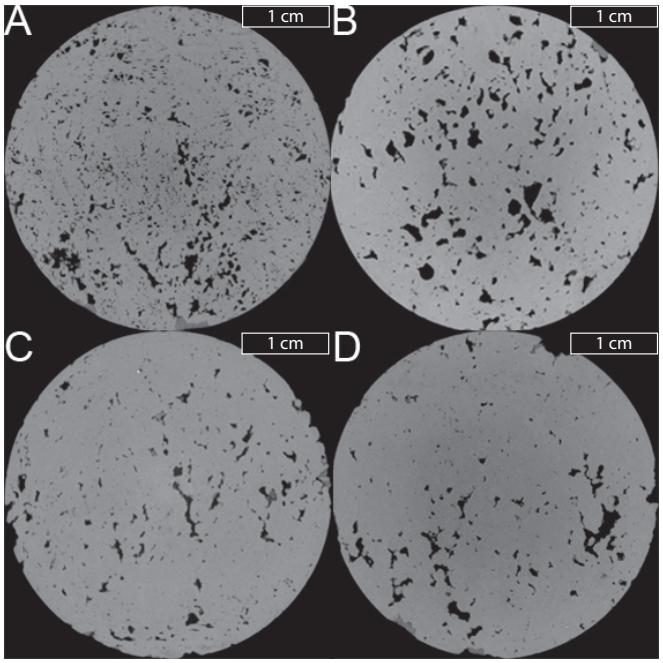


**Figure S1.** µCT slices of each travertine core sample used in this study. A: $LFRLES$; B: $MFRHES$; C: $HFRHES$; D: $HFRLES$. Image size: each slice is 3.8 cm by 3.8 cm.

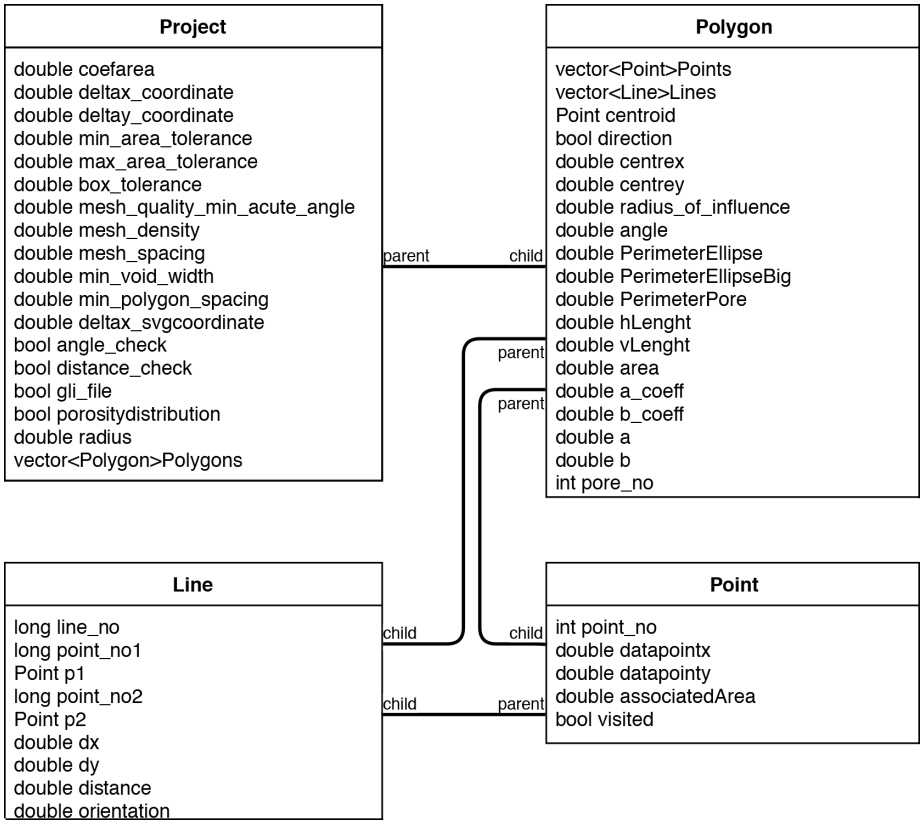


**Figure S2.** Simplified UML diagram presenting the main classes of the ICCR-Macropore, as well as the relationship between them.

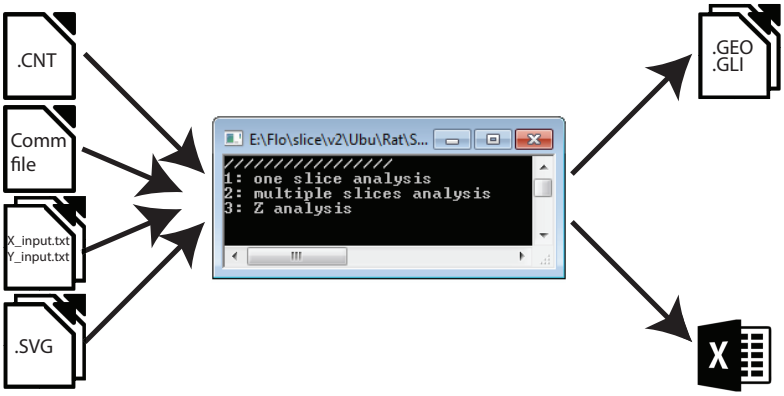


**Figure S3.** General workflow for the ICCR-Macropore. Three input types are necessary (a CNT file, a comm file, a text file, and the SVG pictures). The tool generates three types of output files (mesh file, geo files, and geometrical data).

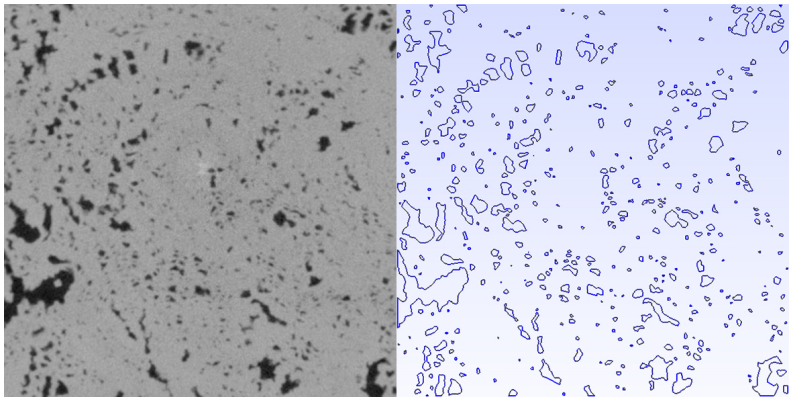

**Figure S4.** Left) Slice from a travertine sample used in this study ($LFRLES$); Right) Isolated porosity after ICCR-Macropore processing.

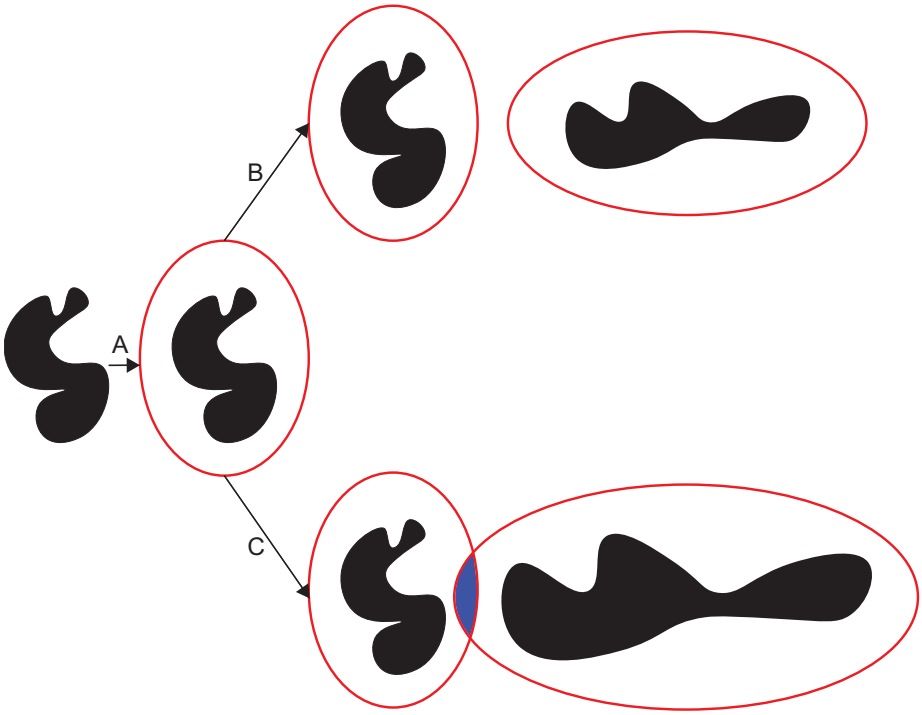


**Figure S5.** Steps for the detection of a link between two pores (black shapes). Step (A) represents the area of influence applied around a pore through a multiplier of the original pore area. The case (B) shows two non-overlapping pores; Case (C) displays a case of overlapping ellipses.


**Figure S8.** Input files of the Slice Picker. The three input units are the ICCR-Macropore, the Slice.txt file, and the Comm file.

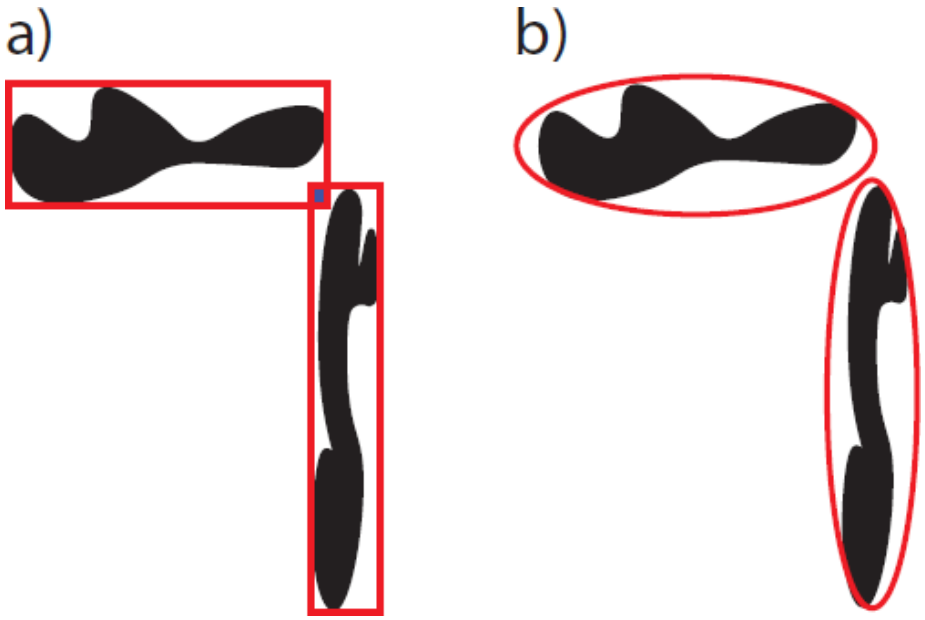


**Figure S6.** Sketch of overlap detection (blue square) between two pores (black) defined by area equivalent of a) rectangles and b) ellipses.

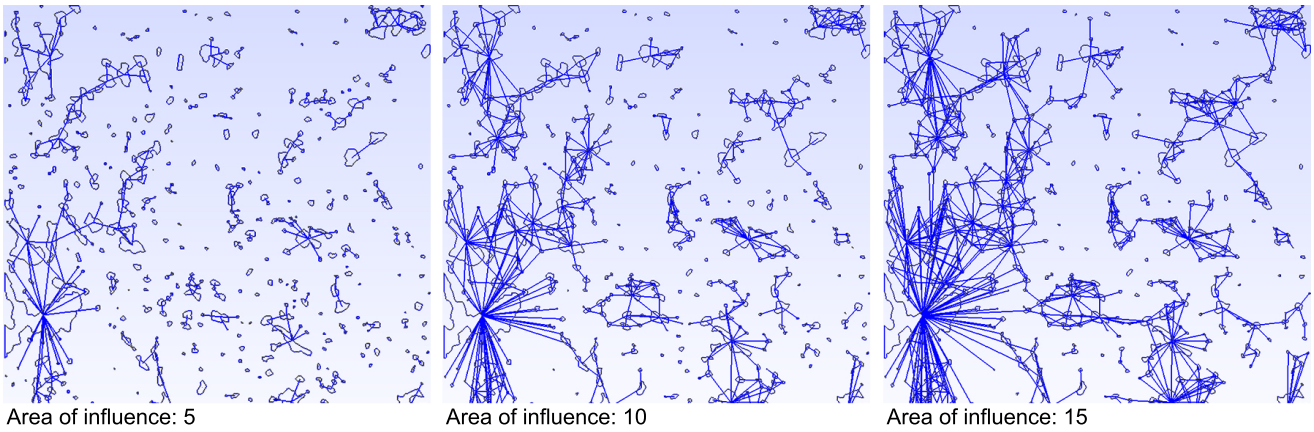


**Figure S7.** Visual rendering of the 2D connections between pores forming a network of interconnected vugs. Three different *area of influence* have been used: 5, 10, and 15.

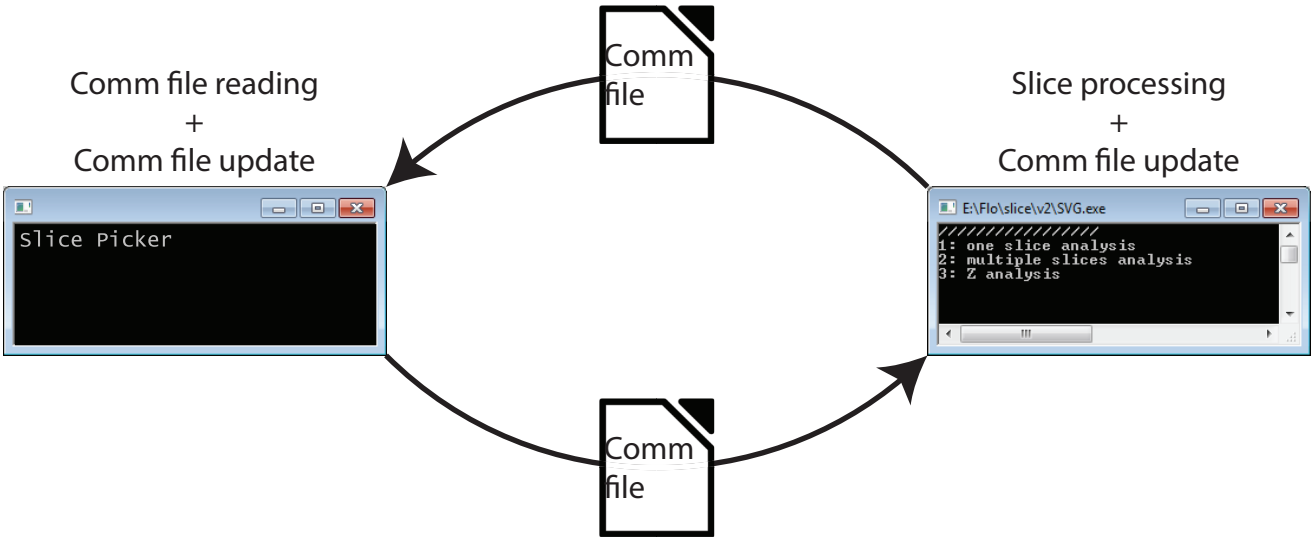


**Figure S9.** Programming logic and communication between the Slice Picker and the ICCR-Macropore. The Comm file is used as an intermediate file.